Precambrian Research 377 (2022) 106736

Contents lists available at ScienceDirect

Precambrian Research

journal homepage: www.elsevier.com/locate/precamres

Local hydrothermal sources for Superior-type iron formations: Insights from the Animikie Basin

Fangbing Li [a], Xiangkun Zhu [a,*], Honglei Ding [a], Kan Zhang [b]

[a] MNR Key Laboratory of Isotope Geology, Institute of Geology, Chinese Academy of Geological Sciences, Beijing, China
[b] State Key Laboratory of Marine Environmental Science, Xiamen University, Fujian, China

ARTICLE INFO

Keywords:
Superior-type IFs
Rare earth elements
Hydrothermal fluids
Animikie Basin

ABSTRACT

Superior-type iron formations (IFs) provide large amounts of iron ore worldwide. Early studies proposed models for Superior-type IFs that involved the delivery of Fe from riverine inputs or from the deep ocean to the outer continental shelf via dynamic upwelling currents. However, the low contents of detritus in IFs and the restricted rate of upwelling in palaeo-oceans do not favour these depositional models for Superior-type IFs. Here, we report major and rare earth element compositions of core samples from Superior-type IFs of late Palaeoproterozoic age from proximal (near-shore) to distal (off-shore) areas of the Animikie Basin in the Lake Superior region, North America. The geochemical characteristics of these IFs, including Eu anomalies and trace element patterns, show that Fe was directly supplied by local hydrothermal exhalative systems rather than by seawater upwelling or continental input. Furthermore, covariation in the Ce anomaly and Fe speciation ratios (Fe_{carb}/Fe_T) suggests that most IFs were deposited close to (but below) the Mn redoxcline, where Fe is easily oxidised, which implies that Fe was locally oxidised without long-distance migration. Accordingly, our study proposes a new model for Superior-type IFs whereby ferrous Fe that is discharged from local hydrothermal vents can be locally and partially oxidised in shallow suboxic areas of a redox-stratified ocean. Enhanced hydrothermal fluxes associated with active mantle plume events are presumed to account for this increased delivery of Fe during the late Palaeoproterozoic.

1. Introduction

Iron formations (IFs) are marine chemical sedimentary rocks composed mainly of iron-rich (15–40 wt% Fe) and siliceous (40–60 wt% SiO_2) layers, beds, or laminates (James, 1954). IFs were deposited mostly between ca. 2.80 and ca. 1.80 Ga (Neoarchean to Palaeoproterozoic), with a minor peak during the Neoproterozoic related to the Snowball Earth event (Klein, 1993; Ilyin, 2009). According to the depositional environment, IFs are broadly classified as being either Algoma-type or Superior-type (Gross, 1980). Algoma-type IFs are typically closely associated with volcanic rocks; therefore, the exhalative–hydrothermal source mode for these IFs is widely accepted (e.g., Gross, 1980). In contrast to Algoma-type IFs, Superior-type IFs are generally associated with carbonate rocks and black shales. Superior-type IFs provide copious amounts of Fe for sustaining modern industrial development, given that these IFs can extend laterally for more than 1000 km in some cases and/or cover large areas exceeding 10^5 km^2 (e.g., IFs in Hamersley, western Australia; Simonson and Goode, 1989). Given the resource provided by Superior-type IFs, the source of the Fe in them has been debated for more than half a century.

On early Earth, the lack of atmospheric oxygen would have stimulated the supply of Fe-rich crust, meaning that a high proportion of dissolved Fe was brought into palaeo-oceans via riverine input. Therefore, early studies proposed a continental Fe source via intense chemical weathering for Superior-type IFs (James, 1954; Cloud, 1968), which was subsequently supported by the Nd isotope signatures of IFs from the Pongola Supergroup [$\varepsilon_{Nd}(t) = -4.3$ to -1.9] (Alexander et al., 2008; Haugaard et al., 2013). However, this proposal has been questioned because of the insufficient river discharge that would have been required to transport the required amount of Fe into the ocean (Holland, 1973; Haugaard et al., 2016; Konhauser et al., 2017). With the discovery of modern seafloor-hydrothermal systems, it has been realised that hydrothermal processes likely made a significant contribution to the oceanic Fe inventory in the modern ocean and that this contribution was presumably more extensive in the palaeo-oceans of early Earth (Bau and Möller, 1993; Tagliabue et al., 2010). Hydrothermally contaminated seawater can be brought into the depositional settings of IFs (e.g., continental shelves) via dynamic upwelling (Trendall and Blockley, 1970).

* Corresponding author.

https://doi.org/10.1016/j.precamres.2022.106736
Received 27 February 2022; Received in revised form 13 May 2022; Accepted 15 May 2022
Available online 25 May 2022
0301-9268/© 2022 Elsevier B.V. All rights reserved.

This upwelling hydrothermally contaminated deep-ocean water has been regarded as the primary source of Fe in Superior-type IFs (e.g., Morris and Horwitz, 1983). The attribution of the upwelling process as the dominant mode of transporting Fe from the deep ocean to the depositional sites of IFs implies that IFs are deposited far from the source of Fe. This model presumes that IFs are formed on a generally isolated and submerged platform (or shelf) on a continental margin, where deep water would have been able to freely circulate, but physical barriers are required to explain the absence of coarse-grained terrigenous clastic sedimentary rocks (Morris, 1993). This model is also problematic because a high rate of upwelling is needed to bring sufficient Fe from the deep sea onto the continental shelf to account for the large amounts of Fe in Superior-type IFs (Konhauser et al., 2007).

To better constrain the source of Fe in Superior-type IFs, it is necessary to establish the spatial pattern of Fe distribution in these formations with respect to proximal and distal positions in the same basin. Assuming that upwelling of hydrothermally contaminated deep water is the dominant source of Fe for Superior-type IFs, it is expected that geochemical characteristics, in particular hydrothermal proxies, should show gradual spatial variation in continuously distributed IF cores (i.e., IFs deposited from shallow to deep ocean; e.g., Lin et al., 2019). For example, the hydrothermal signal is expected to be weaker with increasing distance from mid-ocean ridge (MOR) crests, as hydrothermal fluids discharged from vents on these crests tend to mix with deep-ocean water during transport to depositional sites of Superior-type IFs. IFs in the Animikie Basin of the Lake Superior region (North America)—the type locality of Superior-type IFs in Gross's (1980) classification—provide significant information about the depositional mode of IFs and the evolution of marine redox state during the late Palaeoproterozoic (Poulton et al., 2010; Planavsky et al., 2018). Therefore, in the present study, geological cores located in different depositional environments in the Animikie Basin of the Lake Superior region were selected for detailed investigation. This study focuses mainly on the major element and REE compositions of drill-cores of Superior-type IFs from proximal (near-shore) to distal (off-shore) facies in the Animikie Basin. The results show that spatial variation in the Eu anomalies of different cores indicates that Fe emerging from hydrothermal plumes was supplied directly to depositional sites without long-distance transport caused by mechanisms such as seawater upwelling. On the basis of lateral and vertical variation in Ce anomalies and Fe speciation, we suggest that Fe was partially oxidised as Fe-hydroxides close to (but below) the Mn redoxcline in the late Palaeoproterozoic ocean. A new model is thus proposed for Superior-type IFs, whereby Fe was locally oxidised in suboxic areas while being discharged from local hydrothermal vents. In contrast to previous studies, our study highlights the variation in deposition of IFs as revealed by cores obtained from proximal to distal locations in the basin. The findings of this study have implications for the interplay of hydrothermal activity and oceanic redox state during the late Palaeoproterozoic.

2. Geological background

The Palaeoproterozoic Animikie Basin is located to the northwest of Lake Superior. In ascending stratigraphic order, the basin contains conglomerates of the Kakabeka and Pokegame formations, IFs and chert of the Gunflint Formation in the north of the basin and the Biwabik Formation in the south, and fine-grained sandstones and shales in the Rove and Virginia formations (Davidson and Kor, 1980). The Pokegema and Kakabeka successions were deposited in a high-energy, tidally influenced shoreline environment with an input of terrigenous sediment (e.g., the deposition of sand, pebbles, and gravels). The stratigraphic transition from the Kakabeka and Pokegame conglomerates into the Biwabik and Gunflint IFs represents a transition from a clastic depositional environment to an off-shore environment dominated by chemical precipitation (Miller and Berndt, 2011; Ojakangas et al., 2011). It is almost certain that the shoreline was aligned east–west, to which the sampled cores form a transect at an angle of ~30° (Fig. 1). Here we investigate well-preserved IFs in the Gunflint Formation deposited in the Gunflint Range in the northeastern Animikie Basin and in the Biwabik Formation in the Mesabi Range in the southwestern part of the basin (Ojakangas et al., 2001), encompassing sediments that were deposited up to a distance of ~200 km from the palaeo-shoreline (Poulton et al., 2010).

The Gunflint IFs were deposited on a southward-dipping shelf, in the most distal preserved part of the Animikie Basin. In contrast, the Biwabik IFs were deposited in the proximal part of the basin (Fralick and Barrett, 1995; Pufahl, 1996; Fralick et al., 2002). Superior-type IFs of the Biwabik and Gunflint formations can be divided into five different facies types: four cyclic units classified by cherty and slaty components (lower cherty, lower slaty, upper cherty, and upper slaty, from bottom to top), and the upper capping limestone (Simonson and Goode, 1989; Jirsa et al., 2008; McSwiggen and Morey, 2008; Losh and Rague, 2018). The slaty unit is composed mainly of laminated chemical mudstone consisting of millimetre-thick layers of iron-oxide and chert, representing transgressive deep-water deposition. The cherty unit is characterised by medium-sized grainstone lenses that are composed typically of hematite, magnetite, and chert intraclasts, which are inferred to have been deposited in shallow water where wave- or tide-generated currents formed the grains by reworking fine-grained chemical mudstones. A limestone unit caps the upper member and separates the Gunflint or Biwabik formations from shales of the basal Rove or Virginia formations (Fig. 1). Previous studies have shown that deposition of the Gunflint Formation in a back-arc basin was ongoing at 1878.3 ± 1.3 Ma and had ended by 1849.53 ± 0.21 Ma (Fralick et al., 2002; Davis, 2008), and that the Biwabik Formation was deposited prior to 1850 Ma, as constrained by U–Pb dating of an ash layer in the lower part of the Virginia Formation (Hemming et al., 1995). Therefore, the Biwabik and Gunflint IFs in the Animikie Basin are considered to be coeval based on sequence stratigraphy and geochronology, and thus both record seawater information from the late Palaeoproterozoic.

IFs revealed in the three drill-cores 89-MC-1, MGS-2, and LWD-99 represent an order from near- to off-shore depositional systems in the Animikie Basin. Core 89-MC-1 from the shallower part of the Animikie Basin contains a stratigraphic sequence of IFs of the Gunflint Formation, whereas cores MGS-2 and LWD-99 contain IFs of the Biwabik Formation. Geochemical compositions of core LWD-99 have been reported in earlier studies (Planavsky et al., 2009; 2010) and are discussed here together with new results for cores 89-MC-1 and MGS-2 obtained during this study.

3. Methods

Major element compositions were analysed at the Institute of Geology and Geophysics, Chinese Academy of Sciences, Beijing, China. First, 0.4 g of 200 mesh rock powder, 3 g of lithium tetraborate, and 1 g of lithium metaborate were mixed. Two drops of saturated LiBr were then placed into each of the mixed samples and melted into glass flakes at 1000 °C in a platinum crucible. Finally, samples were measured using an X-ray fluorescence spectrometer (ARL advance XP +). Loss on ignition (LOI) was determined by weight difference. Standard samples BCR-2 and BHVO-2 were used for analytical calibration. Analytical uncertainties on sample major element contents are < 1%.

Trace element contents were analysed using inductively coupled plasma–mass spectrometry (ICP–MS; Agilent 7700e) at the Wuhan Shang Spectral Analysis Technology Co. Ltd test centre, Wuhan, China. Sample processing steps for ICP–MS determinations were as follows: (1) Samples of 200 mesh size were placed in an oven at 105 °C for 12 h. (2) An amount of 50 mg of powder sample was placed into a Teflon sample-dissolving cartridge. (3) An amount of 1 ml of high-purity nitric acid and 1 ml of high-purity hydrofluoric acid were slowly added successively to the powder sample. (4) The Teflon cartridge was inserted into a steel sleeve and heated in an oven at 190 °C for more than 24 h. (5) The

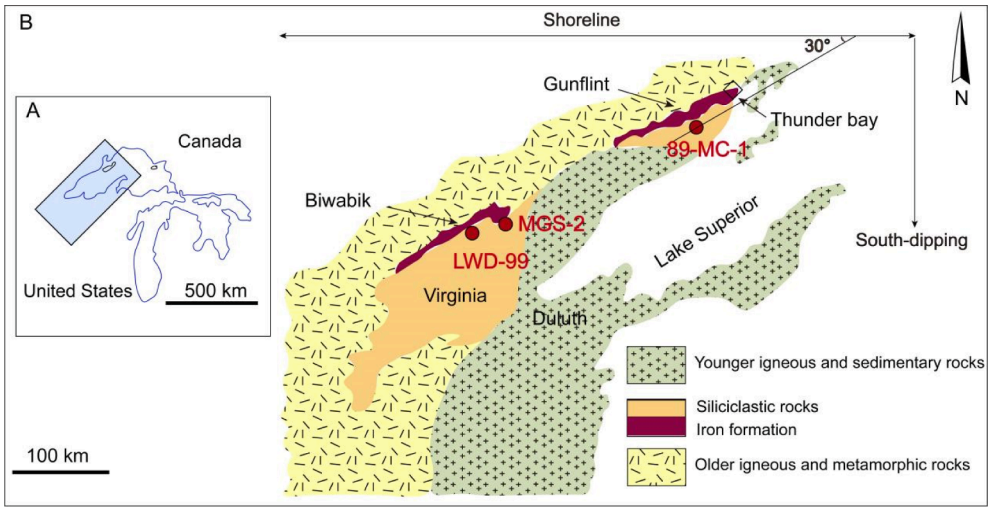

Fig. 1. Geological setting of the Animikie Basin (modified from Poulton, 2010); Fig. 1A: the studied area between the United States and Canada (scale 1: 500000); Fig. 1B: the geographical distribution of the Biwabik and Gunflint Iron Formations. The shoreline was aligned east–west, to which the sampled cores form a transect at an angle of ~30° (Fig. 1). The well-preserved IFs in the Gunflint Formation (89-MC-1) were deposited in the Gunflint Range in the northeastern Animikie Basin, and IFs in the Biwabik Formation (MGS-2 and LWD-99) were deposited in the Mesabi Range in the southwestern part of the basin.

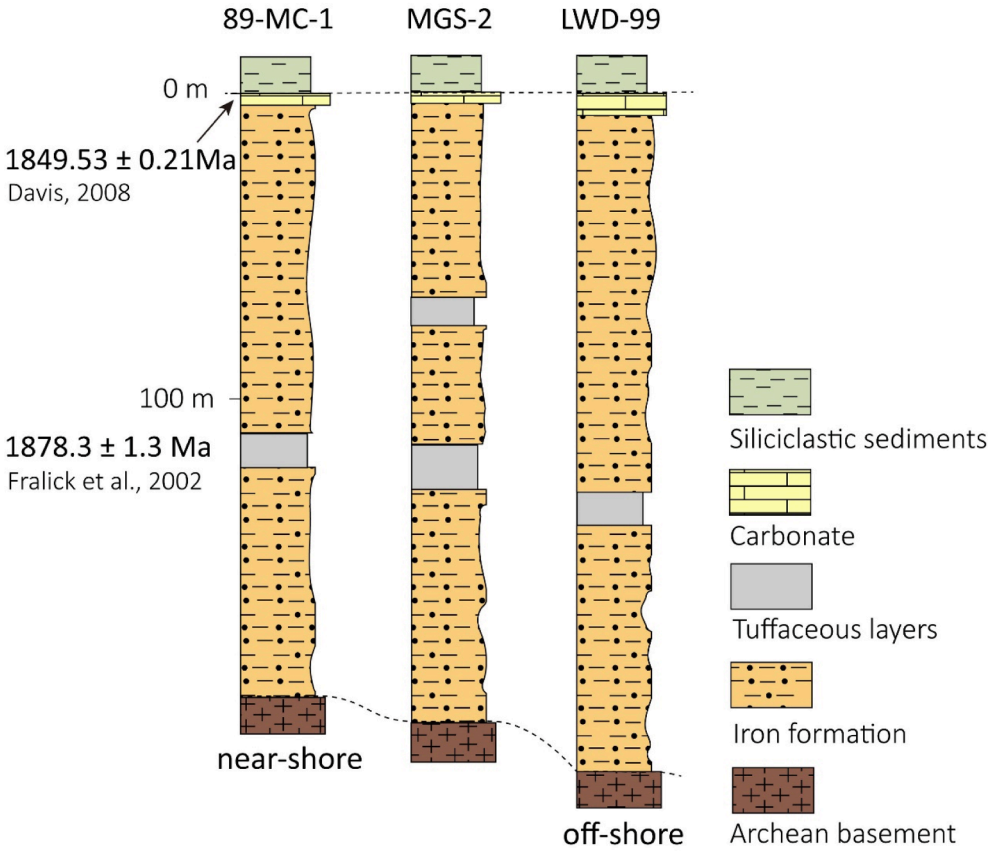

sample and cartridge were cooled to room temperature. After removal from the steel sleeve and opening the lid, the cartridge was placed onto a 140 °C electric heating plate to evaporate the sample to dryness, then 1 ml HNO_3 was added, and the sample was evaporated to dryness again to ensure no remaining liquid in the wall of the cartridge. (6) An amount of 1 ml of high-purity nitric acid, 1 ml MQ water, and 1 ml internal standard (concentration of 1 ppm) were added, following which the Teflon cartridge was reinserted into the steel sleeve, sealed, and heated in an oven at 190 °C for more than 12 h. (7) The resultant solution was transferred into a polyethylene bottle and diluted with 2% HNO_3 to 100 g for ICP–MS analysis. In addition to the samples, two blank samples and four standard samples (BCR-2 and BHVO-2) were prepared for calibration of trace element content analyses.

4. Results

4.1. Major element compositions

The elemental compositions of samples from cores 89-MC-1 and MGS-2 from the Animikie Basin are listed in Tables 1 and 2. Maximum total Fe (as Fe_2O_3) contents of samples from cores 89-MC-1 and MGS-2 are 83.97 wt% and 49.36 wt%, respectively. In the top section of the 89-MC-1, the observed CaO content can reach 38.94 wt%, consistent with the appearance of limestone in the upper section (Fralick et al., 2017). Samples with high contents of Al_2O_3 should be excluded from geochemical and sedimentary interpretation because of the potential contamination from clastic components that tend to contain considerable amounts of REE-bearing minerals, which may compromise the

Table 1
Major, trace element concentration and Fe_{carb}/Fe_T of Ccore 89-MC-1.

Sample	T26	R5	T23	R3	T19	R1	T12	T8	T6	T4	T1	S22	S21	S20	S18
Depth (m)	−1.0	−3.2	−4.5	−6.3	−9.5	−12.0	−15.5	−19.0	−27.0	−41.0	−47.5	−59.5	−67.5	−85.0	−100.5
$Fe_2O_{3Total\ (wt\%)}$	2.65	5.73	27.93	35.26	19.60	24.00	15.19	42.55	51.19	83.97		70.16			
MnO (wt%)	0.72	0.01	0.06	0.86	0.50	0.34	0.03	0.51	0.98	0.18		0.19			
$Al_2O_{3\ (wt\%)}$	0.95	4.54	5.06	4.55	1.97	4.05	2.81	4.89	3.21	0.76		0.91			
$SiO_{2\ (wt\%)}$	23.87	83.99	55.14	40.03	32.38	27.21	75.91	31.92	28.31	6.71		23.13			
CaO (wt%)	38.94	0.16	0.79	1.80	23.27	21.95	0.51	2.98	1.23	3.78		0.85			
MgO (wt%)	0.81	0.92	3.13	3.32	0.93	1.81	1.86	4.24	4.08	0.52		1.19			
LOI	29.83	3.82	6.92	16.25	20.80	21.74	3.72	12.43	11.12	1.24		2.04			
La (ppm)	31.07	4.10	3.23	3.25	13.67	17.73	5.29	8.44	4.53	5.39	4.65	7.46	7.67	3.90	2.84
Ce (ppm)	47.91	8.66	8.78	8.12	29.95	37.38	11.87	31.88	18.03	20.59	15.63	26.22	20.05	13.12	5.91
Pr (ppm)	8.10	0.98	0.73	0.70	2.63	3.60	1.02	1.96	1.08	1.19	1.23	2.07	1.94	0.97	0.56
Nd (ppm)	37.41	3.94	2.86	2.75	9.99	13.19	3.75	7.82	4.26	4.80	5.22	8.81	7.49	3.76	2.02
Sm (ppm)	7.72	0.77	0.54	0.56	1.65	2.27	0.52	1.54	0.99	1.04	1.13	1.85	1.44	0.73	0.34
Eu (ppm)	1.79	0.20	0.15	0.13	0.53	0.60	0.15	0.38	0.25	0.29	0.26	0.59	0.40	0.16	0.07
Gd (ppm)	8.56	0.84	0.60	0.56	1.47	1.86	0.47	1.43	0.94	1.09	1.30	2.10	1.37	0.68	0.31
Tb (ppm)	1.18	0.13	0.09	0.09	0.19	0.23	0.07	0.21	0.14	0.18	0.19	0.34	0.21	0.10	0.05
Dy (ppm)	6.88	0.91	0.59	0.67	0.95	1.29	0.42	1.38	0.90	1.19	1.19	1.88	1.20	0.56	0.27
Y (ppm)	64.31	7.63	4.59	4.34	7.55	8.51	2.90	8.91	5.22	8.42	6.66	13.27	6.65	2.55	1.24
Ho (ppm)	1.40	0.21	0.14	0.14	0.18	0.23	0.09	0.30	0.20	0.24	0.25	0.39	0.25	0.11	0.06
Er (ppm)	3.55	0.63	0.43	0.41	0.47	0.66	0.23	0.91	0.57	0.69	0.66	1.07	0.70	0.30	0.15
Tm (ppm)	0.39	0.09	0.06	0.06	0.06	0.08	0.04	0.13	0.08	0.10	0.08	0.13	0.09	0.04	0.02
Yb (ppm)	2.19	0.59	0.41	0.38	0.34	0.50	0.22	0.85	0.56	0.55	0.44	0.68	0.62	0.23	0.15
Lu (ppm)	0.28	0.10	0.07	0.06	0.05	0.07	0.03	0.13	0.07	0.06	0.06	0.09	0.09	0.03	0.02
Y/Ho	45.89	36.82	33.96	30.75	42.78	36.72	31.11	29.89	26.13	35.82	26.42	34.12	27.02	22.36	21.36
Eu an.	1.15	1.25	1.34	1.14	1.75	1.49	1.50	1.28	1.29	1.33	1.11	1.48	1.41	1.13	1.04
Ce an.	0.81	1.05	1.39	1.35	1.28	1.13	1.27	1.92	1.95	2.07	1.60	1.60	1.18	1.55	1.13
Fe_{carb}/Fe_T	0.17	0.32	0.55	0.26	0.43	0.50	0.34	0.47	0.31	0.22	0.36	0.32	0.11	0.21	0.31
Co (ppm)	9.94	9.48	21.44	23.39	49.18	40.14	12.63	5.51	56.05	11.22	11.66	67.60	56.37	2.73	5.19
Ni (ppm)	31.14	45.98	17.21	11.95	18.30	21.50	11.68	8.02	12.15	6.02	6.54	10.60	14.40	1.10	1.84
Cu (ppm)	9.52	32.50	3.14	5.23	29.92	9.57	10.80	3.27	17.63	0.54	1.62	1.85	13.92	2.94	3.33
Zn (ppm)	221.08	22.45	15.85	19.23	20.19	28.87	11.00	25.42	21.66	5.50	3.51	4.48	20.22	6.51	8.88
Co/Zn	0.04	0.42	1.35	1.22	2.44	1.39	1.15	0.22	2.59	2.04	3.32	15.08	2.79	0.42	0.59
Co + Ni + Cu	50.60	87.96	41.79	40.57	97.40	71.21	35.11	16.80	85.83	17.78	19.83	80.00	84.68	6.77	10.36
Ba (ppm)	14.93	20.93	60.77	22.74	8.18	17.20	77.73	113.31	28.84	28.40	21.66	87.59	31.25	43.44	15.96
Ba/Eu	8.34	104.67	405.16	174.89	15.44	28.66	518.22	298.19	115.36	97.94	83.29	148.45	78.13	271.50	228.04
Zr (ppm)	17.90	71.00	85.90	50.30	24.60	38.00	29.90	86.50	45.40	15.90	15.06	12.10	36.60	9.93	9.65

Table 2
Major, trace element concentration and Fe_{carb}/Fe_T of core MGS-2, BHVO-2 and BCR-2.

Sample	B3	B4	B5	B6	B7	B10	B12	B16	BHVO-2	BCR-2
Depth (m)	−10.0	−13.6	−14.2	−48.1	−48.7	−51.7	−89.5	−113.3		
Fe_2O_{3Total} (wt%)	11.13		14.45	49.36	31.47	36.26	47.89	30.58	12.27	13.65
MnO (wt%)	0.43		0.84	2.00	1.05	0.05	0.07	0.37	0.17	0.19
Al_2O_3 (wt%)	0.12		0.56	0.22	0.29	0.04	0.17	0.62	13.47	13.28
SiO_2 (wt%)	13.57		17.14	19.70	55.65	62.50	46.62	52.37	49.79	53.74
CaO (wt%)	26.21		24.24	8.23	0.40	0.16	0.17	0.62	11.37	7.14
MgO (wt%)	11.96		9.59	3.59	1.13	0.38	2.84	6.78	7.21	3.56
LOI	36.13		33.61	17.36	10.25	0.14	1.54	8.30		
La (ppm)	5.54	3.18	3.03	3.47	0.59	0.31	0.78	12.46	15.20	24.90
Ce (ppm)	7.09	5.51	5.74	7.10	1.29	0.72	1.92	25.68	37.20	52.90
Pr (ppm)	0.97	0.60	0.64	0.80	0.16	0.10	0.20	3.36	5.22	6.70
Nd (ppm)	3.69	2.35	2.42	3.23	0.75	0.50	0.84	13.67	24.20	28.70
Sm (ppm)	0.71	0.49	0.50	0.63	0.16	0.11	0.18	2.70	5.84	6.58
Eu (ppm)	0.28	0.17	0.16	0.20	0.05	0.03	0.05	0.65	2.07	1.96
Gd (ppm)	0.88	0.66	0.68	0.75	0.16	0.12	0.21	2.25	6.09	6.75
Tb (ppm)	0.14	0.13	0.11	0.11	0.04	0.02	0.03	0.28	0.96	1.07
Dy (ppm)	0.94	0.99	0.79	0.77	0.21	0.11	0.22	1.47	5.44	6.41
Y (ppm)	10.61	9.10	7.42	6.00	1.48	0.59	1.38	7.73	26.10	37.00
Ho (ppm)	0.22	0.25	0.17	0.17	0.04	0.03	0.04	0.25	0.97	1.28
Er (ppm)	0.66	0.76	0.56	0.50	0.13	0.06	0.13	0.62	2.53	3.66
Tm (ppm)	0.09	0.10	0.07	0.07	0.02	0.01	0.02	0.07	0.35	0.54
Yb (ppm)	0.64	0.69	0.44	0.37	0.14	0.05	0.12	0.39	2.03	3.38
Lu (ppm)	0.10	0.10	0.07	0.05	0.02	0.01	0.02	0.06	0.28	0.50
Y/Ho	49.09	36.42	43.63	34.82	35.64	23.41	33.57	30.46		
Eu an.	1.81	1.44	1.41	1.51	1.32	1.28	1.35	1.37		
Ce an.	0.82	1.06	1.00	1.06	1.12	1.07	1.19	0.92		
Fe_{carb}/Fe_T	0.74	0.78	0.79	0.37	0.42	0.92	0.11	0.45		
Co (ppm)	3.88	3.21	3.12	5.43	1.42	0.75	4.37	5.26	44.70	37.00
Ni (ppm)	14.12	4.50	7.52	5.27	5.52	6.43	4.55	5.64	124.00	13.00
Cu (ppm)	4.67	1.22	2.31	1.10	1.44	2.34	1.09	2.36	127.00	18.40
Zn (ppm)	6.10	10.38	8.54	4.65	4.60	2.27	4.42	15.65	107.00	133.00
Co/Zn	0.64	0.31	0.37	1.17	0.31	0.33	0.99	0.34		
Co + Ni + Cu	22.67	8.93	12.95	11.80	8.38	9.52	10.01	13.26		
Ba (ppm)	7.81	7.80	6.71	15.74	9.01	14.31	4.55	3.68	128.00	669.00
Ba/Eu	27.91	45.88	41.94	78.72	180.26	476.98	90.94	5.67		
Zr (ppm)	4.49	7.63	6.47	6.17	5.29	1.37	3.43	10.80	172.00	188.00

geochemical information from seawater recorded in IFs. For the samples discussed below, there is no discernible covariation between Al_2O_3 and REE contents, which suggests negligible terrigenous clastic impacts on ΣREEs (Fig. 2). In this study, the Mn contents (MnO) of IF samples are low (<1 wt%), consistent with previous studies that found much lower Mn contents in well-preserved carbonate rocks or IFs of Proterozoic age relative to Archaean counterparts (Veizer et al., 1989). The low Mn contents of our samples may have been a result of (1) low aqueous concentrations of Mn in the palaeo-ocean, and/or (2) the difficulty of precipitation and enrichment of Mn in the suboxic to anoxic marine environment.

4.2. Trace element and REE compositions

Significant differentiation in the relative contents of Co, Cu, Ni, and Zn has been identified for hydrothermal and normal/hydrogenetic authigenic sediments (Toth, 1980). The samples analysed in this study show low values of Co/Zn (mean of ~ 0.80) and Co + Ni + Cu (6.77–97.40 ppm) (Fig. 3), implying that the studied chemical sedimentary rocks formed in an environment dominated by hydrothermal activity. It is noted that analysis of Eu contents in low-REE samples suffers from the interference of BaO, often leading to "false positives" in normalised patterns that suggest the presence of a positive Eu anomaly. The ratio of Ba/Eu can be used to differentiate interference from BaO; a Ba/Eu ratio of < 1000 indicates that a positive Eu anomaly is not an analytical artifact arising from insufficient correction of Ba (Shabani et al., 1992) (Tables 1 and 2).

The contents of Zr in sedimentary rocks are affected mainly by terrigenous clastic input, meaning that Zr (ppm) can be used as a proxy for terrigenous input during the depositional period. The contents of Zr in samples from MGS-2 (1.37–10.80 ppm) and LWD-99 (<60 ppm) are lower than those in 89-MC-1 (9.65–86.50 ppm). However, even for the samples in 89-MC-1 with higher Zr contents, there is no significant positive or negative covariation between Zr (ppm) and REEs (ppm), Eu/Eu*, Y/Ho, and Ce/Ce*, which implies that the clastic contribution to patterns of REEs is negligible (Fig. 2a, d, g, and j). In addition to possible clastic contribution/input, post-depositional process (e.g., diagenetic fluids) may also have an effect on compositional characteristics of REEs in sedimentary rocks (Webb and Kamber, 2000; Lin et al., 2011). However, previous studies of Palaeoproterozoic Kuruman IFs have identified immobile behaviour of REEs during post-depositional processes owing to the large ionic radius of most REEs, resulting in distinct REE compositions between iron-rich and silica-rich bands (Bau, 1993; Bau and Möller, 1993; Morris, 1993). This is a strong argument in favour of closed-system conditions for REEs in IFs, whereby a low water–rock reaction rate controls the inactivity/immobility of REEs during post-depositional processes such as metamorphism and deformation.

Rare earth element (REEs) compositions of IFs were normalised with respect to post-Archaean Australian shale (PAAS; Tables 1 and 2) (Taylor and McLennan, 1981). In this study, Ce and Eu anomalies were calculated as $Ce/Ce^* = Ce/[Pr \times (Pr/Nd)]$, and $Eu/Eu^* = Eu/(0.67 \times Sm + 0.33 \times Tb)$, respectively (Lawrence and Kamber, 2006). PAAS-normalised REE distribution patterns for samples from core 89-MC-1 are characterised by (1) LREE enrichment; (2) positive Eu anomalies, with $(Eu/Eu^*)_{PAAS}$ ranging from 1.04 to 1.75; and (3) positive Ce anomalies, with $(Ce/Ce^*)_{PAAS}$ varying from 0.81 to 2.07 (Fig. 4). PAAS-normalised REEs distribution patterns for samples from core MGS-2 are characterised by (1) positive Eu anomalies, with $(Eu/Eu^*)_{PAAS}$ ranging from 1.28 to 1.81; and (2) weak negative or positive Ce anomalies, with $(Ce/Ce^*)_{PAAS}$ varying from 0.82 to 1.19 (Fig. 4).

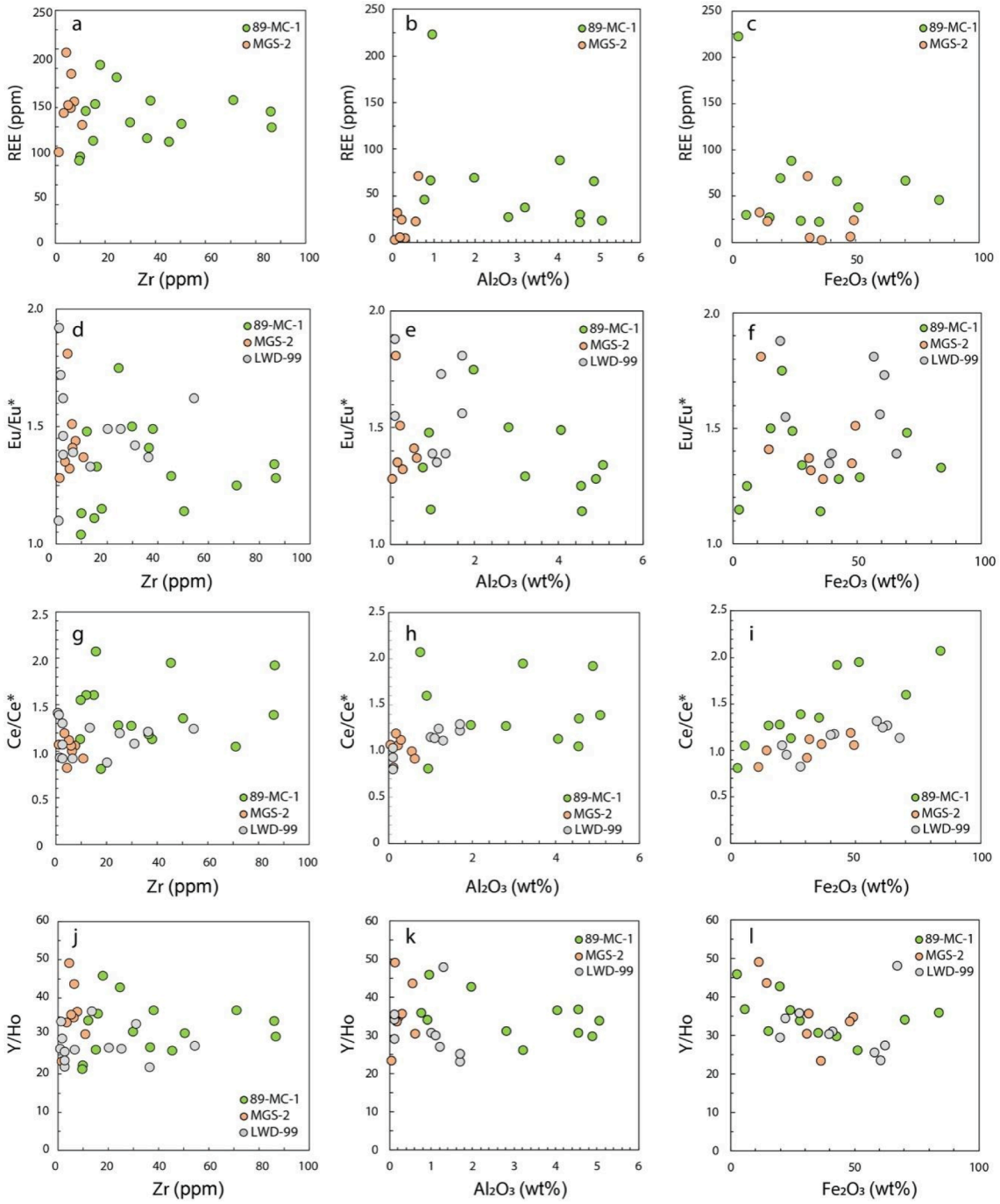

Fig. 2. Cross-plots of (a) Zr (ppm) v.s. REEs (ppm), (b) Al_2O_3 (wt%) v.s. REEs (ppm), (c) Fe_2O_3 (wt%) v.s. REE (ppm), (d) Zr (ppm) v.s. Eu/Eu*, (e) Al_2O_3 (wt%) v.s. Eu/Eu*, (f) Fe_2O_3 (wt%) v.s. Eu/Eu*, (g) Zr (ppm) v.s. Ce/Ce*, (h) Al_2O_3 (wt%) v.s. Ce/Ce*, (i) Fe_2O_3 (wt%) v.s. Ce/Ce*, (j) Zr (ppm) v.s. Y/Ho, (k) Al_2O_3 (wt%) v.s. Y/Ho, and (l) Fe_2O_3 (wt%) v.s. Y/Ho in core 89-MC-1, MGS-2 and LWD-99. All samples have minor and rare earth element compositions (major elemental contents are not reported in some samples in core 89-MC-1, MGS-2 and LWD-99), and thus figure a, d, g and j contain all samples referred in this study.

5. Discussion

5.1. Hydrothermal signals in IFs

Along with geological processes such as aeolian dust and submarine groundwater discharge, the net river flux is considered to have been one of the main sources of REEs in palaeo-oceans (Kim and Kim, 2011; Deng et al., 2017), as coagulated and suspended clay particles transported by large palaeo-river networks commonly adsorb large amounts of REEs. To evaluate the detrital contribution to REEs in the Animikie Basin, we investigated the relationship between proxies of clastic enrichment (i.e., contents of Al_2O_3 and Zr) and REEs (i.e., Eu/Eu* and Ce/Ce*) (Fig. 2). It is expected that higher terrigenous input should promote the enrichment of REEs in chemical sediments. However, the absence of a positive covariation between Zr (and/or Al_2O_3) and total REEs (ΣREEs) reveals a negligible contribution from clastic materials to the ΣREE budget (Fig. 2a and b). In addition, the lack of an inverse trend between Zr (and/or Al_2O_3) and Eu/Eu* (Fig. 2d and e) indicates a negligible effect of contamination by clastic materials. However, the contents of Zr and Al_2O_3 in 89-MC-1 (proximal or near-shore) are higher than those in MGS-2 and LWD-99 (distal or off-shore), meaning that values of Eu/Eu* in 89-MC-1 may have been affected by clastic materials. Compared with

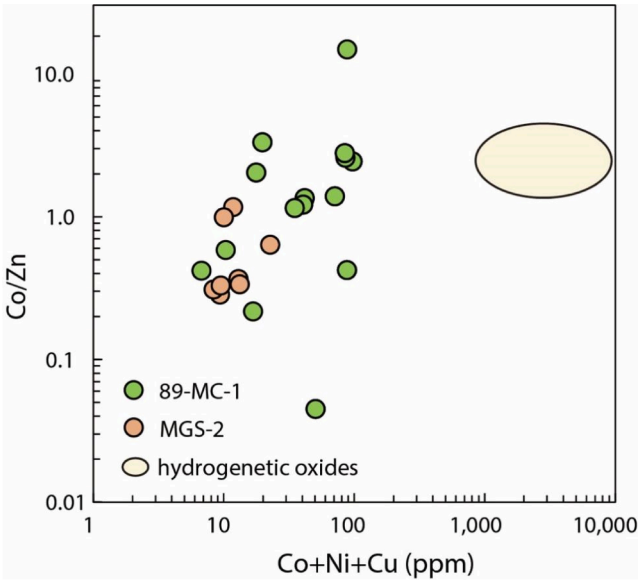

Fig. 3. Relationship between Co/Zn and (Co + Ni + Cu) of 89-MC-1, MGS-2 and hydrogenetic oxides. Low Co/Zn and (Co + Ni + Cu) indicate a hydrothermal source of IFs in Animikie Basin. It is possible that a rapid precipitation of hydrothermal oxides (e.g., IFs) precludes the surface complexation onto Fe (hydro)oxides from trace (and rare earth) elements. Hydrogenetic oxides data are from Pelleter et al., 2017.

MGS-2 and LWD-99, the higher contents of detritus in 89-MC-1 may mask the geochemical characteristics from hydrothermal solutions and thus result in lowered values of Eu/Eu*. However, all of the samples from core 89-MC-1 possess positive Eu anomalies, which suggests that hydrothermal pulses were the dominant influence on IFs from this core. It should be noted that this interpretation does not imply that the content of Fe provided by hydrothermal vents should have a positive relationship with REEs or Eu anomalies (Fig. 2c and f). Covariation relationships between Fe_2O_3 and ΣREEs and Eu/Eu* reflect the capacity of REEs to be adsorbed onto suspended and dissolved iron oxyhydroxides in seawater, which is influenced predominantly by factors such as sedimentation rate, the size of oxyhydroxide particulates, and fluctuation in the redox condition of ambient seawater.

Chemical sedimentary rocks recording hydrothermal signals are typically characterised by strong positive Eu anomalies after normalisation with respect to PAAS. This geochemical indicator can thus be used to differentiate whether chemical sedimentary rocks were derived from a hydrothermal source, but should be carefully used for samples in early Earth's oceans. PAAS-normalised positive Eu anomalies are common in Archaean carbonate rocks (Kamber and Webb, 2001; Bekker et al., 2010; Planavsky et al., 2010), suggesting that Archaean seawater was globally enriched in Eu. In contrast, Palaeoproterozoic seawater was not enriched in Eu (Danielson et al., 1992; Bau and Alexander, 2006; Schier et al., 2018; Wang et al., 2018). The absence of positive Eu anomalies in Palaeoproterozoic carbonate rocks, such as magnesite deposits (ca. 1.8 Ga) in Ceará in northeastern Brazil (Parente et al., 2004), limestones in the Rooinekke and Nelani formations (ca. 2.4 Ga) in South Africa (Schier et al., 2018), and the lack of LREE enrichment in carbonate rocks of the Chilpi Group (2.0–1.8 Ga) in India (Mishra and Mohanty, 2021) rule out a substantial influence of hydrothermal solutions on the chemistry of Palaeoproterozoic seawater. The disappearance of Eu enrichment in seawater from the Archaean to the Palaeoproterozoic has been investigated by previous studies. For example, Viehmann et al. (2015) found that positive Eu anomalies in seawater showed a substantial decrease from 2.5 Ga using compiled REE data for 755 pure marine chemical sedimentary rocks (Viehmann et al., 2015). Furthermore, even if it is assumed that Palaeoproterozoic seawater was characterised by positive Eu anomalies, the Eu anomalies of Palaeoproterozoic seawater would have been low due to dilution with ambient seawater, and homogeneous because of dynamic oceanic circulation, in theory resulting in weak but consistently positive Eu anomalies being recorded in marine chemical sedimentary rocks. However, contemporaneous samples in the three IF cores from the Animikie Basin have widely diverse positive $(Eu/Eu^*)_{PAAS}$ values, which could not have been inherited from the homogenous Eu content expected from marine thermohaline circulation in the ocean. Therefore, it is highly likely that the positive Eu anomalies of IFs from the Animikie Basin were derived from hydrothermal exhalative systems rather than from the chemical characteristics of Palaeoproterozoic seawater.

In addition to Eu anomalies, other proxies such as trace element content ratios (e.g., Co/Zn) (Toth, 1980) and REE ratios (e.g., Sm/Yb) (Alexander et al., 2008) can be used to differentiate whether chemical deposits were contaminated by hydrothermal vents and to assess whether the involved hydrothermal vents were of a high- or low-temperature nature. For example, in hydrothermally derived sediments, Co shows typically pronounced depletion relative to Cu and Ni, but Zn is largely enriched, resulting in characteristically low Co/Zn (~0.15) values. In contrast, hydrogenetic deposits without a hydrothermal influence would involve more Co from ambient seawater via incorporation and adsorption onto hydroxides, with elevated Co/Zn ratios (~2.50) in these deposits (Toth, 1980; Salem et al., 2016; Pelleter et al., 2017). As shown in Fig. 3, the low Co/Zn ratios (mean of ~ 0.80) and depleted Co, Ni, and Cu contents (<100 ppm) of samples from IFs of the Animikie Basin support a hydrothermal source (Fig. 3). The covariation between Sm/Yb and Eu/Sm indicates that IFs in the Animikie Basin were formed predominantly by mixing of seawater and low-

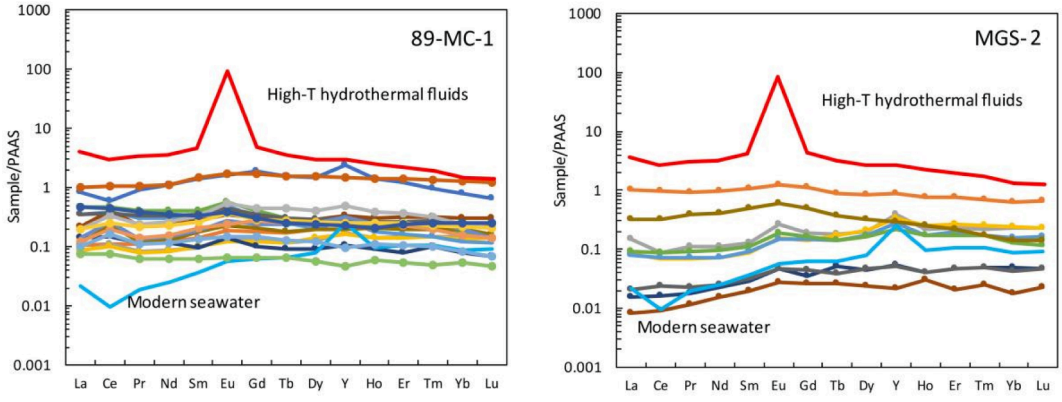

Fig. 4. PAAS-normalized REEs distribution patterns of core 89-MC-1 and MGS-2. Average compositions of hydrothermal fluids (Bau and Dulski, 1999) and of modern seawater (Zhang and Nozaki, 1996) are also shown in the figure.

temperature hydrothermal solutions (Fig. 5).

5.2. Local hydrothermal source of Fe

If it were assumed that Fe was delivered to the shallow continental shelf via upwelling after being discharged from hydrothermal vents in MORs, proxies related to the level of hydrothermal intensity (e.g., Eu anomalies) should decrease gradually from distal to proximal IFs (i.e., with increasing distance from ancient hydrothermal vents) owing to the further mixing between the oceanic water mass and hot submarine hydrothermal exhalation along the upwelling trajectory. However, the observed positive Eu anomalies of the proximal IFs (core 89-MC-1), with a mean Eu/Eu* value of 1.30, are of similar size to those of the distal IFs (cores MGS-2 and LWD-99). In particular, the highest Eu anomaly value (1.75) is recorded in the top 10 m of core 89-MC-1, which shows higher values than those of the corresponding layer in the two distal IF cores (MGS-2 and LWD-99) (Fig. 6). Therefore, the lack of a progressive decrease in the size of positive Eu anomalies from deep-water (MGS-2 and LWD-99) to shallow-water (89-MC-1) IFs is not consistent with Fe being delivered predominantly from the deep ocean to the outer continental shelf by upwelling currents from a MOR system.

Alternatively, it is possible that the Fe in the studied IF cores was sourced from local hydrothermal vents, consistent with the observed similar size of positive Eu anomalies in the different cores. This pattern, rather than a broad decrease in Eu anomaly from deeper to shallower (off-shore to near-shore), suggests that Fe was introduced rapidly and locally into shallow waters by nearby developing plumes rather than undergoing long-distance migration from submarine hydrothermal plumes at a MOR to shallow-water regions via upwelling (Bau and Möller, 1993; Haugaard et al., 2016). Given this proposed scenario, it is difficult to determine the number or volume of discharge of hydrothermal vents, which presumably occurred with several sporadic pulses. If an exclusive local hydrothermal vent (contaminated with seawater) had served as the source of Fe input into the basin, the variation in positive Eu anomalies would be expected to be laterally consistent between the three cores. For example, Eu/Eu* values show values of 1.00–1.15 in the 100–80 m depth range in 89-MC-1, above which they increase to 1.40–1.50 at around 60 m depth, and increasing from 1.30 to 1.75 then decreasing to 1.15 in the 20–0 m depth range. These patterns of variation in Eu/Eu* are not observed for cores LWD-99 and MGS-2. Thus, the variations in positive Eu anomalies between the three cores

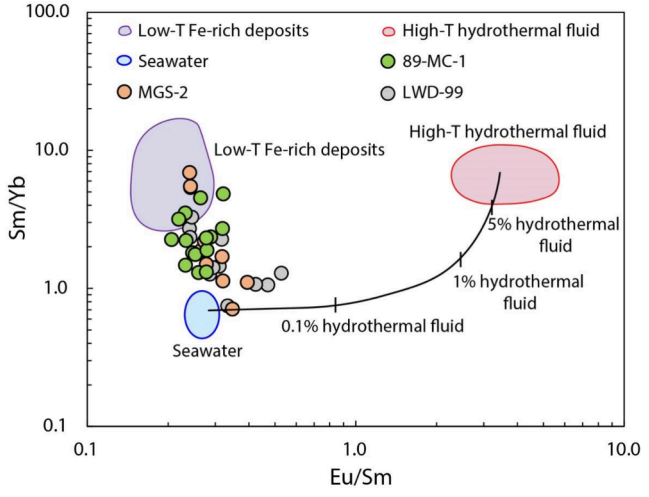

Fig. 5. Plots of Sm/Yb and Eu/Sm of 89-MC-1, MGS-2 and LWD-99. IFs in Animikie Basin are associated with low-T hydrothermal systems. High-temperature hydrothermal fluids data are according to Bau and Dulski (1999), and low-temperature Fe-rich deposits and Pacific seawater are from Alibo and Nozaki (1999).

are distinct and asynchronous, implying that the Eu anomalies of sedimentary rocks from these three cores were dominated by contributions from independent hydrothermal vents. The waxing and waning of these local hydrothermal vents resulted in the temporal (i.e., depth) variation in the size of positive Eu anomalies in the IF cores.

5.3. Near-source oxidation of Fe

The element Ce is particularly prone to fractionate relative to other REEs because the oxidation of Ce (III) to Ce (IV) under oxidising conditions greatly reduces the solubility of Ce, resulting in its preferential removal from solution onto Mn (IV)–Fe (III) oxyhydroxides (Elderfield, 1988; German and ElderField, 1990; Quinn et al., 2004; 2006). Hence, anomalies in the normalised abundance of Ce, designated as Ce/Ce*, are commonly used to quantify the degree of decoupling of Ce relative to its neighbouring REEs and to fingerprint the redox conditions of palaeo-seawater. Accordingly, the occurrence of negative Ce anomalies (Ce/Ce* < 1.00) in chemical sedimentary rocks (e.g., iron formations and carbonate rocks) has often been used to infer oxidative conditions during deposition (Alibo and Nozaki, 1999; Dellwig et al., 2010; Chen et al., 2015). The dissolution of metal oxyhydroxides occurring across the redoxcline will lead to an increase in the Ce concentration of the local seawater, and in turn, a positive Ce anomaly (Ce/Ce* greater than 1.00) is typically shown by Fe–Mn hydroxide or oxide particles that are responsible for the scavenging adsorption (Bau and Möller, 1993; Loope et al., 2013).

In the present study, positive Ce anomalies increase from 1.13 (100.5 m depth) to 2.07 (41.0 m depth) and then decrease to ~1.00 near the top of 89-MC-1, except for the uppermost carbonate sample, which shows a negative Ce anomaly (Ce/Ce* = 0.81; Fig. 7). The pattern of variation in Fe_{carb}/Fe_T for core 89-MC-1 is almost reverse to that of Ce/Ce*, with a reduction from 0.31 to 0.22 (100.5 to 41.0 m depth) in the lower part of the core and increasing to ~ 0.55 (4.5 m depth) in the top part (Poulton et al., 2010). An almost reverse covariation between the Ce anomaly (from 0.82 to 1.19) and Fe_{carb}/Fe_T (from 0.11 to 0.92) is also observed in core MGS-2. These variations from bottom to top in Ce anomaly values are similar to those reported from core LWD-99, which range from 0.81 to 1.41 (Fig. 7). Therefore, lower Fe_{carb}/Fe_T ratios (or higher Fe_2O_3 contents, Fig. 2i) are associated with higher Ce anomalies for samples of equivalent depositional depth within each core. This covariation in Fe speciation and Ce anomalies for different IFs indicates that Fe oxyhydroxides, with their high sorption capacity, may be dominant captors of Ce from the ocean. However, unlike oxidative scavenging by Mn oxyhydroxides, it would appear that the incorporated Ce onto Fe oxyhydroxides was in a dissolved state in the palaeo-ocean. Although this difference may have been lessened by a higher level of oxygenation of the ocean, for example, a previous study of modern ferromanganese crusts from the central Pacific has suggested that oxidative scavenging of Ce is not confined to Mn oxides but also occurs on hydrous Fe oxides in the natural marine system (Bau and Koschinsky, 2009). However, Ce/Ce* values of marine carbonate rocks and modelling of atmospheric oxygen level (pO_2) together suggest Paleoproterozoic atmospheric oxygen concentrations were low (0.1 ~ 1% of the present atmospheric level) (Bellefroid et al., 2018; Liu et al., 2021). Therefore, the incorporation of Ce onto Fe oxyhydroxides in IFs involved a dissolved state, especially in the suboxic to anoxic marine conditions of the Palaeoproterozoic. Hence, the relationship between Fe speciation (Fe_{carb}/Fe_T ratios) (Poulton et al., 2010) and Ce anomalies in IFs of low Mn content (MnO < 1 wt%) from the Animikie Basin reflects the massive amount of dissolved Ce released by the reduction of Mn oxyhydroxides below the Mn redoxcline and captured by Fe oxyhydroxides. Higher positive Ce anomalies in IFs signify that the depositional sites were initially closer to (but below) the Mn redoxcline, where Mn oxyhydroxides were almost completely reduced but ferrous Fe was easily oxidised, meaning that Fe oxyhydroxides were able to capture the Ce released from Mn oxyhydroxides. In this scenario, on the one hand, the

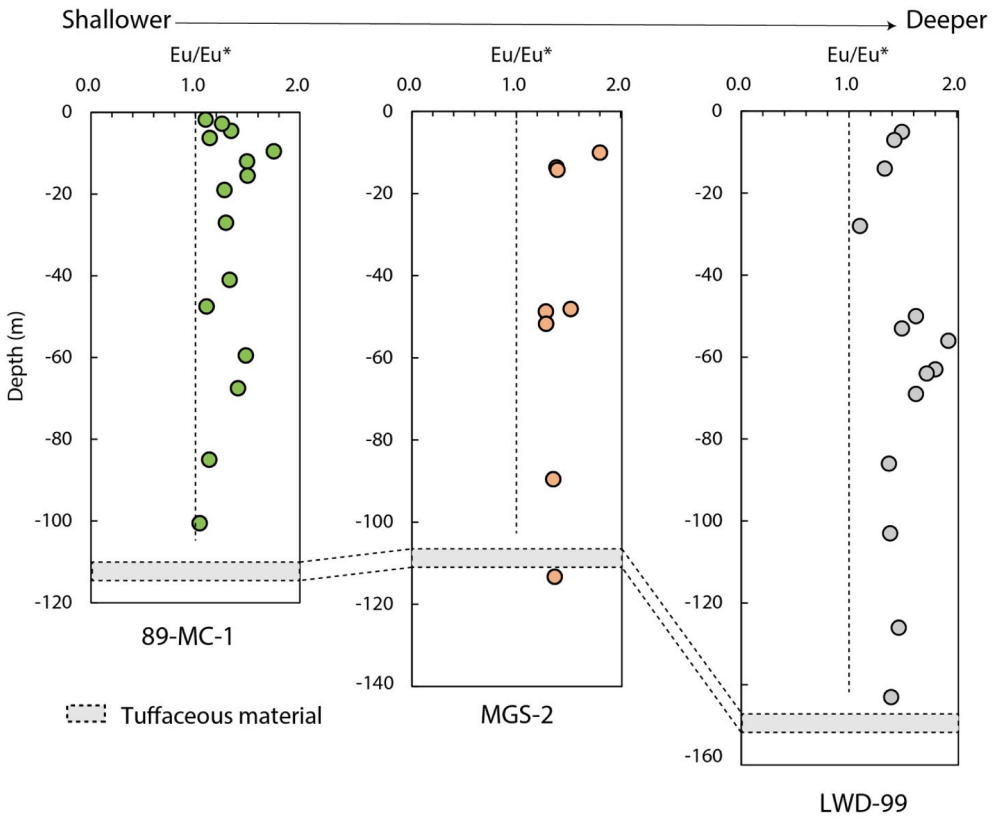

Fig. 6. Variations of PAAS normalized Eu anomalies with depths in core IFs from 89-MC-1, MGS-2 and LWD-99. The absence of progressive decrease on Eu anomalies from the off- to near-shore IFs challenged the upwelling-origin iron model for Superior-type IFs.

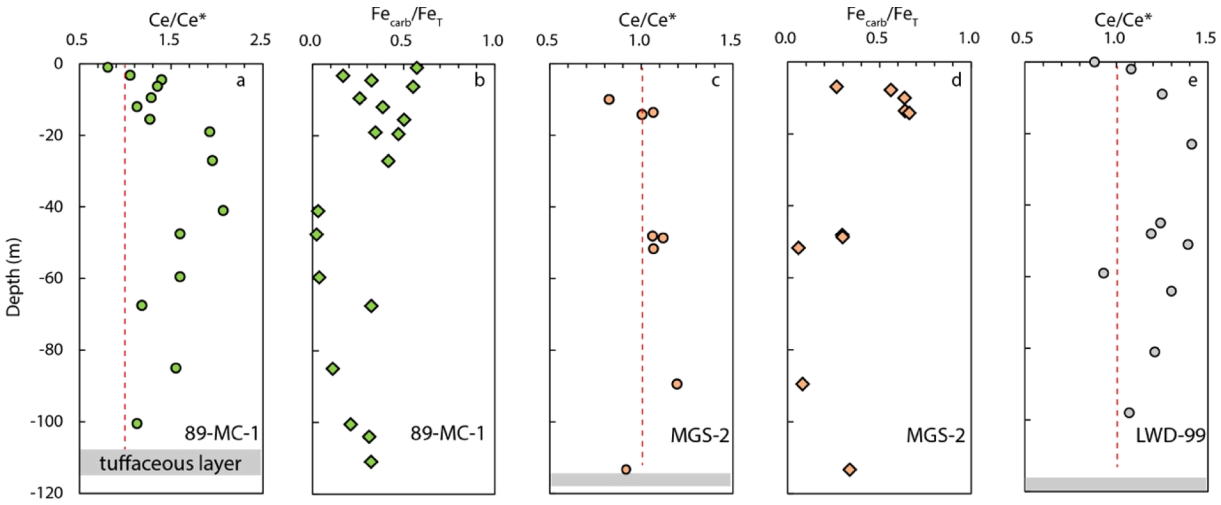

Fig. 7. Variations of Ce/Ce* and Fe_{carb}/Fe_T with depths of core 89-MC-1 (a,b), MGS-2 (c,d) and LWD-99 (e, Fe speciation data are not reported). The coupled (reverse) variation between Fe_{carb}/Fe_T and Ce anomalies in core 89-MC-1 and MGS-2 reveals that Fe depositional sites were initially closer to (but below) the Mn redoxcline and later farther below it.

vertical variation in Ce anomaly in IF cores from the Animikie Basin suggests that Fe depositional sites were initially closer to (but below) the Mn redoxcline and later farther below it. On the other hand, most IFs with prominent positive Ce anomalies suggest that their depositional sites were close to the Mn redoxcline, where Fe was easily oxidised. In this framework, Fe was able to be deposited immediately near the hydrothermal source in the form of Superior-type IFs without long-distance transport, with the extent of oxidation depending on the change in the position of the marine redoxcline.

This model is also supported by the synchronous variation in Y/Ho ratios of three IF cores in the Animikie Basin. It is expected that a low or even near-chondritic Y/Ho ratio would be observed in chemical sedimentary rocks because Ho is considerably more particle reactive than Y with respect to being scavenged onto adsorptive particles such as Mn–Fe oxyhydroxides, organic matter, and clay minerals (Bau and Dulski, 1994; Bau et al., 1997). Like Ce, the redox recycling of Mn oxyhydroxides is also a key influence on the pronounced fractionation between Y and Ho in the marine environment, despite their coherent

behaviour caused by the similar ionic radius and charge of these two elements. Late Palaeoproterozoic IFs in the Animikie Basin show a vertical trend in Y/Ho ratio from bottom to top (Fig. 8) that is consistent with the variation in Ce anomalies (Figs. 7, 2i and l). This variation indicates that depositional sites of IFs first were close to (but below) the Mn redoxcline and captured more released Ho from the dissolution of settling Mn-rich oxyhydroxide particles in the suboxic water column, resulting in low Y/Ho values in the lower part of IF cores (average = 28.60, 128.0 to 41.0 m depth). Then, the depositional sites were father below the Mn redoxcline, with less Ho captured by IFs and an upward-increasing Y/Ho trend on the top section. As most of the IF samples of this study show low Y/Ho ratios, the studied depositional sites of IFs may have been located close to the Mn redoxcline. During the deposition of IFs, it is considered that Fe released from hydrothermal vents would be oxidised immediately without long-distance transport in the region close to (but below) the Mn redoxcline. In other words, a local oxidation mechanism is suggested for the IFs in the Animikie Basin.

5.4. A new depositional model for Superior-type IFs

James (1954) first proposed that ferrous Fe was supplied to the ocean by continental weathering under an anoxic atmosphere and then sequestered as ferric (hydro)oxides by reaction with free oxygen generated by cyanobacteria in the near-surface ocean. This model was modified by Cloud (1973), who suggested periodic transport of ferrous Fe into the photic zone by overturning caused by variation in climate. The source of Fe was considered as continental riverine input until the recognition of the close temporal association between the source of Fe in IFs and volcanic activity (Trendall and Blockley, 1970). With the identification of positive Eu anomalies in many Superior-type IFs, it was increasingly acknowledged that the Fe in IFs had been derived primarily from submarine hydrothermal fluids (rather than from the weathering of continental rocks) and subsequently delivered to oxic shallow near-shore areas via seasonal upwelling (Jacobsen and Pimentel-Klose, 1988; Klein and Beukes, 1992; Holland and Petersen, 1995). In such a case, the source of Fe could have been distal MOR systems. This model for Superior-type IFs has become widely accepted, although unsolved problems remain regarding the mechanism of dynamic upwelling systems. For example, based on the amount of Fe in an annual micro-band from the IFs in Hamersley Basin, northwestern Australia, the rate of upwelling required would have been one magnitude higher than that of the modern coastal environment (Trendall, 1972). Accordingly, the conventional model involving upwelling along the coastline does not appear to account for the amount of Fe required for the large volumes of Superior-type IFs. Furthermore, upwelling is a result of wind, which varies seasonally; however, detailed sampling of the Hamersley IFs at various scales has shown that the amount of Fe in the deposits is invariant over periods of 1 to 1000 y, indicating the absence of seasonal control (Li et al., 2015).

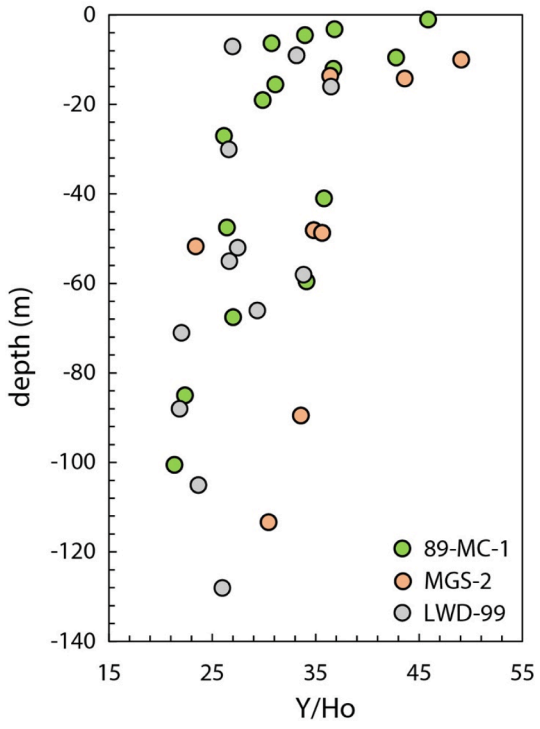

Fig. 8. Variation of Y/Ho with depths in 89-MC-1, MGS-2 and LWD-99.

Here, we propose a new model for the formation of Superior-type IFs based on the geochemical characteristics of IFs in the Animikie Basin of the Lake Superior region. In this model, Fe was sourced from local hydrothermal fluids without long-distance transport and was precipitated in suboxic areas of a redox-stratified ocean in the form of Superior-type IFs, with the extent of oxidation depending on the change in the position of the marine redoxcline (Fig. 9). It might seem that there is a contradiction in this model, in that most of the hydrothermal activity in oceans is confined to MOR crests in deeper parts of the modern water column, whereas depositional sites of IFs are located predominantly along continental shelves. However, previous studies have shown that hydrothermal venting can occur in both modern and palaeo-shallow water, such as the Azores, Loihi, and Xuanlong (Karl et al., 1988; Couto et al., 2015; Zhu et al., 2022). It has also been reported that shallow hydrothermal vents were more prevalent in early Earth's ocean, when Earth's interior had cooled enough for the mantle to form (Baross and Hoffman, 1985). In fact, the close association between Superior-type IFs and hydrothermal systems in the late Palaeoproterozoic ocean has not only been found in the Animikie Basin but also in the Frere IFs (1.88 Ga) of western Australia (Walter et al., 1976; Akin et al., 2013; Shellnutt et al., 2018; Parashuramulu et al., 2021), the Sokoman IFs (1.88 Ga) of Canada (Knoll and Simonson, 1981), and the Duck Creek Dolomite (1.8 Ga) of western Australia (Knoll and Barghoorn, 1976; Wilson et al., 2010). These active hydrothermal vents prevalent in Palaeoproterozoic basins are considered to have been manifestations of the well-documented ca. 1885 Ma mafic–ultramafic magmatic activity, one of the most massive igneous episodes in Earth's history, which was characterised by the large-scale mantle plume activity in individual continents (Heaman et al., 1986; Halls and Heaman, 2000; French et al., 2008; Rasmussen et al., 2012; Ciborowski et al., 2017; Samal et al., 2019). In conclusion, our new results and proposed model provide novel insights into the deposition of Superior-type IFs in the Precambrian ocean, whereby even if the upwelling of deep-ocean water was not dynamic, Fe that was discharged in hydrothermal solutions could still be deposited locally as IFs near vents.

6. Conclusion

Early studies proposed a model for the formation of Superior-type IFs whereby Fe is delivered from riverine input or from the deep ocean to the outer continental shelf via dynamic upwelling ocean currents. However, low contents of detritus in Superior-type IFs and the limited rate of upwelling in the palaeo-ocean preclude these depositional models for Superior-type IFs. To better constrain the source of Fe for Superior-type IFs, we investigated the elemental compositions and Fe speciation of samples of Superior-type IFs taken from cores in proximal (near-shore) to distal (off-shore) locations within the late Palaeoproterozoic Animikie Basin. Geochemical evidence from Eu anomalies and trace element contents suggest that the Fe in Superior-type IFs was sourced from local hydrothermal exhalative systems. Furthermore, covariation in Ce anomalies and Fe speciation suggests that the depositional sites of most IFs were close to (but below) the oceanic Mn redoxcline, where Mn oxyhydroxides are almost completely reduced but ferrous Fe is easily oxidised. Accordingly, we propose a new model for

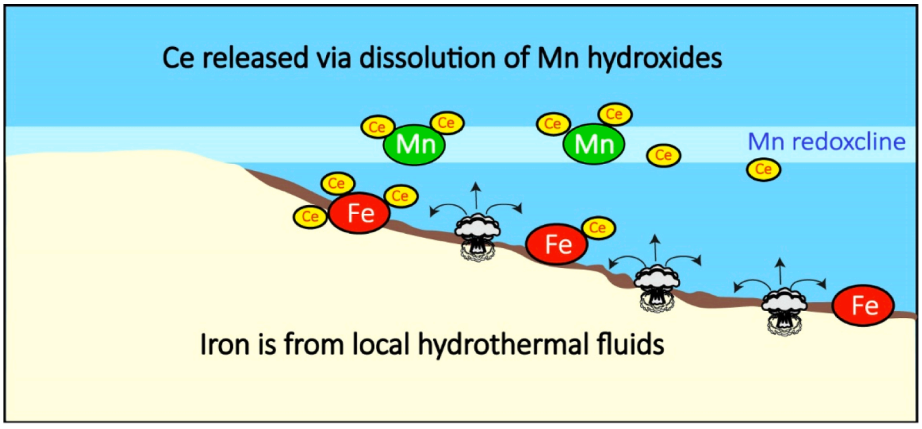

Fig. 9. Schematic diagram for depositional model of Superior-type IFs in Animikie Basin. Iron was oxidised in a suboxic state after deriving from local hydrothermal vents without long-distance migration in the late Palaeoproterozoic ocean.

Superior-type IFs, whereby Fe can be locally (and partially) oxidised in shallow suboxic areas after being derived from local hydrothermal vents without long-distance migration. The increased hydrothermal circulation associated with the active mantle plume events at ca. 1.8 Ga presumably accounted for the enhanced Fe delivery during the late Palaeoproterozoic.

CRediT authorship contribution statement

Fangbing Li: Project administration, Writing – review & editing, Funding acquisition. **Xiangkun Zhu:** Supervision, Conceptualization, Funding acquisition, Writing – review & editing. **Honglei Ding:** Formal analysis, Investigation. **Kan Zhang:** Formal analysis, Investigation.

Declaration of Competing Interest

The authors declare that they have no known competing financial interests or personal relationships that could have appeared to influence the work reported in this paper.

Acknowledgements

We thank Drs. Philip W. Fralick, Simon W. Poulton and Donald E. Canfield for providing samples, and Jin Li, Yao Shi, Zhihong Li and Jian-Xiong Ma for their guidance during the chemical experiments at CAGS. This study was financially supported by National Natural Science Foundation of China (41873027, 4210030382, 42103019), the National Key R&D Programs of China (2019YFA0708404), and Key Laboratory of Deep-Earth Dynamics of Ministry of Natural Resources (J1901-20-1).

References

Akin, S.J., Pufahl, P.K., Hiatt, E.E., Pirajno, F., Sheldon, N., 2013. Oxygenation of shallow marine environments and chemical sedimentation in Palaeoproterozoic peritidal settings: Frere Formation, Western Australia. Sedimentology 60 (7), 1559–1582.
Alexander, B.W., Bau, M., Andersson, P., Dulski, P., 2008. Continentally-derived solutes in shallow Archean seawater: Rare earth element and Nd isotope evidence in iron formation from the 2.9 Ga Pongola Supergroup, South Africa. Geochim. Cosmochim. Acta 72 (2), 378–394.
Alibo, D.S., Nozaki, Y., 1999. Rare earth elements in seawater: Particle association, shale-normalization, and Ce oxidation. Geochim. Cosmochim. Acta 63 (3-4), 363–372.
Baross, J.A., Hoffman, S.E., 1985. Submarine hydrothermal vents and associated gradient environments as sites for the origin and evolution of life. Orig. Life Evol. Biosph. 15 (4), 327–345.
Bau, M., 1993. Effects of syn- and post-depositional processes on the rare-earth element distribution in Precambrian iron-formations. Eur. J. Mineral. 5 (2), 257–268.
Bau, M., Alexander, B., 2006. Preservation of primary REE patterns without Ce anomaly during dolomitization of Mid-Paleoproterozoic limestone and the potential re-establishment of marine anoxia immediately after the"Great Oxidation Event". S. Afr. J. Geol. 109, 81–86.
Bau, M., Dulski, P., 1994. Evolution of the yttrium-holmium systematics of seawater through time. Mineral. Mag. 58 A(1), 61–62.
Bau, M., Dulski, P., 1999. Comparing yttrium and rare earths in hydrothermal fluids from the Mid-Atlantic Ridge: implications for Y and REE behaviour during near-vent mixing and for the YrHo ratio of Proterozoic seawater. Chem. Geol. 155, 77–90.
Bau, Michael, Koschinsky, Andrea, 2009. Oxidative scavenging of cerium on hydrous Fe oxide: Evidence from the distribution of rare earth elements and yttrium between Fe oxides and Mn oxides in hydrogenetic ferromanganese crusts. Geochem. J. 43 (1), 37–47.
Bau, M., Möller, P., 1993. Rare earth element systematics of the chemically precipitated component in early precambrian iron formations and the evolution of the terrestrial atmosphere-hydrosphere-lithosphere system. Geochim. Cosmochim. Acta 57 (10), 2239–2249.
Bau, M., Möller, P., Dulski, P., 1997. Yttrium and lanthanides in eastern Mediterranean seawater and their fractionation during redox-cycling. Mar. Chem. 56 (1-2), 123–131.
Bekker, A., Slack, J.F., Planavsky, N., Krapez, B., Hofmann, A., Konhauser, K.O., Rouxel, O.J., 2010. Iron Formation: The Sedimentary Product of a Complex Interplay among Mantle, Tectonic, Oceanic, and Biospheric Processes. Econ. Geol. 105 (3), 467–508.
Bellefroid, E.J., Hood, A.v.S., Hoffman, P.F., Thomas, M.D., Reinhard, C.T., Planavsky, N. J., 2018. Constraints on Paleoproterozoic atmospheric oxygen levels. Proc Natl Acad Sci U S A 115 (32), 8104–8109.
Chen, J., Algeo, T.J., Zhao, L., Chen, Z.-Q., Cao, L., Zhang, L., Li, Y., 2015. Diagenetic uptake of rare earth elements by bioapatite, with an example from Lower Triassic conodonts of South China. Earth Sci. Rev. 149, 181–202.
Ciborowski, T.J.R., Minifie, M.J., Kerr, A.C., Ernst, R.E., Baragar, B., Millar, I.L., 2017. A mantle plume origin for the Palaeoproterozoic Circum-Superior Large Igneous Province. Precambr. Res. 294, 189–213.
Cloud, P.E., 1968. Atmospheric and hydrospheric evolution on the primitive earth. Science 160 (3829), 729–736.
Cloud, P.E., 1973. Paleoecological significance of the banded iron-formation. Econ. Geol. 68, 1135–1143.
Couto, R.P., Rodrigues, A.S., Neto, A.I., 2015. Shallow-water hydrothermal vents in the Azores (Portugal). Revista de Gestão Costeira Integrada 15 (4), 495–505.
Danielson, A., Möller, P., Dulski, P., 1992. The europium anomalies in banded iron formations and the thermal history of the oceanic crust. Chem. Geol. 97 (1-2), 89–100.
Davidson, R.J., Kor, P.S.G., 1980. Protecting Ontario's ancient fossil record: schrelber channel provincial nature reserve and Kakabeka falls provincial park Geocscience Canada 7, 118–120.
Davis, D.W., 2008. Sub-million-year age resolution of Precambrian igneous events by thermal extraction–thermal ionization mass spectrometer Pb dating of zircon: Application to crystallization of the Sudbury impact melt sheet. Geology 36 (5), 383. https://doi.org/10.1130/G24502A.110.1130/2008094.
Dellwig, O., Leipe, T., März, C., Glockzin, M., Pollehne, F., Schnetger, B., Yakushev, E.V., Böttcher, M.E., Brumsack, H.-J., 2010. A new particulate Mn–Fe–P-shuttle at the redoxcline of anoxic basins. Geochim. Cosmochim. Acta 74 (24), 7100–7115.
Deng, Y., Ren, J., Guo, Q., Cao, J., Wang, H., Liu, C., 2017. Rare earth element geochemistry characteristics of seawater and porewater from deep sea in western Pacific. Sci Rep 7 (1), 16539.
Elderfield, H., 1988. The Oceanic Chemistry of the Rare-Earth Elements. Philos. Trans. R. Soc. Lond. 325, 105–124.
Fralick, P., Barrett, T.J., 1995. Depositional controls on iron formation associations in Canada. Sedimentary Facies Analysis: A Tribute to the Research and Teaching of Harold G. In: Plint, A.G. (Ed.), Sedimentary Facies Analysis. Blackwell Publishing Ltd., Oxford, UK, pp. 137–156. https://doi.org/10.1002/9781444304091.ch6.
Fralick, P., Davis, D.W., Kissin, S.A., 2002. The age of the Gunflint Formation, Ontario, Canada: single zircon U-Pb age determinations from reworked volcanic ash. Can. J. Earth Sci. 39 (7), 1085–1091.

Fralick, P., Planavsky, N., Burton, J., Jarvis, I., Addison, W.D., Barrett, T.J., Brumpton, G. R., 2017. Geochemistry of Paleoproterozoic Gunflint Formation carbonate: Implications for hydrosphere-atmosphere evolution. Precambr. Res. 290, 126–146.
French, J.E., Heaman, L.M., Chacko, T., Srivastava, R.K., 2008. 1891–1883Ma Southern Bastar-Cuddapah mafic igneous events, India: A newly recognized large igneous province. Precambr. Res. 160 (3–4), 308–322.
German, C.R., Elderfield, H., 1990. Application of the Ce anomaly as a paleoredox indicator: The ground rules. Paleoceanography 5 (5), 823–833.
Gross, G.A., 1980. A classification of iron formations based on depositional environments. Can. Mineral. 18, 215–222.
Halls, H.C., Heaman, L.M., 2000. The paleomagnetic significance of new U-Pb age data from the Molson dyke swarm, Cauchon Lake area, Manitoba. Can. J. Earth Sci. 37 (6), 957–966.
Haugaard, R., Frei, R., Stendal, H., Konhauser, K., 2013. Petrology and geochemistry of the ~2.9 Ga Itilliarsuk banded iron formation and associated supracrustal rocks, West Greenland: Source characteristics and depositional environment. Precambr. Res. 229, 150–176.
Haugaard, R., Pecoits, E., Lalonde, S., Rouxel, O., Konhauser, K., 2016. The Joffre banded iron formation, Hamersley Group, Western Australia: Assessing the palaeoenvironment through detailed petrology and chemostratigraphy. Precambr. Res. 273, 12–37.
Heaman, L.M., Machado, N., Krogh, T.E., Weber, W., 1986. Precise U-Pb zircon ages for the Molson dyke swarm and the Fox River sill: Constraints for Early Proterozoic crustal evolution in northeastern Manitoba, Canada. Contrib Mineral Petrol 94 (1), 82–89.
Hemming, S.R., McLennan, S.M., Hanson, G.N., 1995. Geochemical and Nd/Pb Isotopic Evidence for the Provenance of the Early Proterozoic Virginia Formation, Minnesota. Implications for the Tectonic Setting of the Animikie Basin. J. Geol. 103 (2), 147–168.
Holland, H.D., 1973. The Oceans: A Possible Source of Iron in Iron-Formations. Econ. Geol. 68 (7), 1169–1172.
Holland, H.D., Petersen, U., 1995. Living dangerously: Princeton. New Jersey Princeton University Press, p. 490.
Ilyin, A.V., 2009. Neoproterozoic banded iron formations. Lithol. Min. Resour. 44 (1), 78–86.
Jacobsen, S.B., Pimentel-Klose, M.R., 1988. A Nd isotopic study of the Hamersley and Michipicoten banded iron formations: the source of REE and Fe in Archean oceans. Earth Planet. Sci. Lett. 87 (1-2), 29–44.
James, H.L., 1954. Sedimentary facies of iron-formation. Econ. Geol. 49 (3), 235–293.
Jirsa, M.A., Miller, J.D., Morey, G.B., 2008. Geology of the Biwabik Iron Formation and Duluth Complex. Regul Toxicol Pharmacol 52 (1), S5–S10.
Kamber, B.S., Webb, G.E., 2001. The geochemistry of late Archaean microbial carbonate: Implications for ocean chemistry and continental erosion history. Geochim. Cosmochim. Acta 65 (15), 2509–2525.
Karl, D.M., McMurtry, G.M., Malahoff, A., Garcia, M.O., 1988. Loihi Seamount, Hawaii: a mid-plate volcano with a distinctive hydrothermal system. Nature 335 (6190), 532–535.
Kim, I., Kim, G., 2011. Large fluxes of rare earth elements through submarine groundwater discharge (SGD) from a volcanic island. Jeju. Korea. Mar. Chem. 127 (1-4), 12–19.
Klein, C., 1993. Sedimentology and Geochemistry of the Glaciogenic Late Proterozoic. Econ. Geol. 88, 542–565.
Klein, C., Beukes, N.J., 1992. Proterozoic iron-formations. Developments in Precambrian Geology 10, 383–418.
Knoll, A.H., Barghoorn, E.S., 1976. A Gunflint-Type Microbiota From The Duck Creek Dolomite. Western Australia. Origins of Life 7 (4), 417–423.
Knoll, A.H., Simonson, B., 1981. Early Proterozoic Microfossils and Penecontemporaneous Quartz Cementation in the Sokoman Iron Formation. Canada. Science 211 (4481), 478–480.
Konhauser, K.O., Amskold, L., Lalonde, S.V., Posth, N.R., Kappler, A., Anbar, A., 2007. Decoupling photochemical Fe(II) oxidation from shallow-water BIF deposition. Earth Planet. Sci. Lett. 258 (1-2), 87–100.
Konhauser, K.O., Planavsky, N.J., Hardisty, D.S., Robbins, L.J., Warchola, T.J., Haugaard, R., Lalonde, S.V., Partin, C.A., Oonk, P.B.H., Tsikos, H., Lyons, T.W., Bekker, A., Johnson, C.M., 2017. Iron formations: A global record of Neoarchaean to Palaeoproterozoic environmental history. Earth Sci. Rev. 172, 140–177.
Lawrence, M.G., Kamber, B.S., 2006. The behaviour of the rare earth elements during estuarine mixing—revisited. Mar. Chem. 100 (1-2), 147–161.
Li, W., Beard, B.L., Johnson, C.M., 2015. Biologically recycled continental iron is a major component in banded iron formations. Proc Natl Acad Sci U S A 112 (27), 8193–8198.
Lin, Y., Tang, D., Shi, X., Zhou, X., Huang, K., 2019. Shallow-marine ironstones formed by microaerophilic iron-oxidizing bacteria in terminal Paleoproterozoic. Gondwana Res. 76, 1–18.
Lin, Z., Wang, Q., Feng, D., Liu, Q., Chen, D., 2011. Post-depositional origin of highly 13C-depleted carbonate in the Doushantuo cap dolostone in South China: Insights from petrography and stable carbon isotopes. Sed. Geol. 242 (1-4), 71–79.
Liu, X.M., Kah, L.C., Knoll, A.H., Cui, H., Wang, C., Bekker, A., Hazen, R.M., 2021. A persistently low level of atmospheric oxygen in Earth's middle age. Nat Commun 12 (1), 351.
Loope, G.R., Kump, L.R., Arthur, M.A., 2013. Shallow water redox conditions from the Permian-Triassic boundary microbialite: The rare earth element and iodine geochemistry of carbonates from Turkey and South China. Chem. Geol. 351, 195–208.
Losh, S., Ragues, R., 2018. Hydrothermal oxidation in the Biwabik Iron Formation, MN, USA. Miner. Deposita 53 (8), 1143–1166.
McSwiggen, P.L., Morey, G.B., 2008. Overview of the mineralogy of the Biwabik Iron Formation, Mesabi Iron Range, northern Minnesota. Regul Toxicol Pharmacol 52 (1), S11–S25.
Miller, J., Berndt, M., 2011. Mineralogy, spatial distribution, and isotope geochemistry of sulfide minerals in the Biwabik iron formation.
Mishra, P.K., Mohanty, S.P., 2021. Geochemistry of carbonate rocks of the Chilpi Group, Bastar Craton, India: Implications on ocean paleoredox conditions at the late Paleoproterozoic Era. Precambr. Res. 353, 106023. https://doi.org/10.1016/j.precamres.2020.106023.
Morris, R.C., 1993. Genetic modelling for banded iron-formation of the Hamersley Group, Pilbara Craton. Western Australia. Precambrian Research 60 (1-4), 243–286.
Morris, R.C., Horwitz, R.C., 1983. The origin of the iron formation-rich Hamersley Group of Western Australia. Precambrian Res 21, 273–297.
Ojakangas, R.W., Severson, M.J., Jongewaard, P.K., 2011. Geology and sedimentology of the Paleoproterozoic Animikie Group: The Pokegama Formation, the Biwabik Iron Formation, and Virginia Formation of the eastern Mesabi Iron Range and Thomson Formation near Duluth, northeastern Minnesota, Archean to Anthropocene: Field Guides to the Geology of the Mid-Continent of North America, pp. 101-120.
Ojakangas, R.W., Morey, G.B., Southwick, D.L., 2001. Paleoproterozoic basin development and sedimentation in the Lake Superior region, North America. Sed. Geol. 141-142, 319–341.
Parashuramulu, V., Shankar, R., Sarma, D.S., Nagaraju, E., Babu, N.R., 2021. Baddeleyite Pb-Pb geochronology and paleomagnetic poles for ~1.89–1.86 Ga mafic intrusions from the Dharwar craton, India, and their paleogeographic implications. Tectonophysics 805, 228789. https://doi.org/10.1016/j.tecto.2021.228789.
Parente, C.V., Ronchi, L.H., Sial, A.N., Guillou, J.J., Arthaud, M.H., Fuzikawa, K., Veríssimo, C.U.V., 2004. Geology and geochemistry of paleoproterozoic magnesite deposits (~1.8Ga), State of Ceará, Northeastern Brazil. Carbonates Evaporites 19 (1), 28–50.
Pelleter, E., Fouquet, Y., Etoubleau, J., Cheron, S., Labanieh, S., Josso, P., Bollinger, C., Langlade, J., 2017. Ni-Cu-Co-rich hydrothermal manganese mineralization in the Wallis and Futuna back-arc environment (SW Pacific). Ore Geol. Rev. 87, 126–146.
Planavsky, N., Bekker, A., Rouxel, O.J., Kamber, B., Hofmann, A., Knudsen, A., Lyons, T. W., 2010. Rare Earth Element and yttrium compositions of Archean and Paleoproterozoic Fe formations revisited: New perspectives on the significance and mechanisms of deposition. Geochim. Cosmochim. Acta 74 (22), 6387–6405.
Planavsky, N., Rouxel, O., Bekker, A., Shapiro, R., Fralick, P., Knudsen, A., 2009. Iron-oxidizing microbial ecosystems thrived in late Paleoproterozoic redox-stratified oceans. Earth Planet. Sci. Lett. 286 (1-2), 230–242.
Planavsky, N.J., Slack, J.F., Cannon, W.F., O'Connell, B., Isson, T.T., Asael, D., Jackson, J.C., Hardisty, D.S., Lyons, T.W., Bekker, A., 2018. Evidence for episodic oxygenation in a weakly redox-buffered deep mid-Proterozoic ocean. Chem. Geol. 483, 581–594.
Poulton, S.W., Fralick, P.W., Canfield, D.E., 2010. Spatial variability in oceanic redox structure 1.8 billion years ago. Nat. Geosci. 3 (7), 486–490.
Pufahl, P.K., 1996. Stratigraphic architecture of a paleoproterozoic iron formation depositional system : the Gunflint, Mesabi and Cuyuna iron ranges. Lakehead University, Thunder Bay, Ont. Unpublished M.Sc. thesis.
Quinn, K.A., Byrne, R.H., Schijf, J., 2004. Comparative Scavenging of Yttrium and the Rare Earth Elements in Seawater: Competitive Influences of Solution and Surface Chemistry. Aquat. Geochem. 10 (1/2), 59–80.
Quinn, K.A., Byrne, R.H., Schijf, J., 2006. Sorption of yttrium and rare earth elements by amorphous ferric hydroxide: Influence of solution complexation with carbonate. Geochim. Cosmochim. Acta 70 (16), 4151–4165.
Rasmussen, B., Fletcher, I.R., Bekker, A., Muhling, J.R., Gregory, C.J., Thorne, A.M., 2012. Deposition of 1.88-billion-year-old iron formations as a consequence of rapid crustal growth. Nature 484 (7395), 498–501.
Salem, I.A., El-Shibiny, N.H., Monsef, M.A., 2016. Mineralogical and Geochemical Studies on Manganese Deposits at Abu Ghusun Area, South Eastern Desert. Egypt. Journal of Geography and Earth Sciences 4 (2). https://doi.org/10.15640/jges10.15640/jges.v4n2a4.
Samal, A.K., Srivastava, R.K., Gautam, G.C., 2019. Paleoproterozoic (~1.88–1.89 Ga) ultramafic–mafic sills, Cuddapah basin, India—revisited: Implications for interaction between mantle plume and metasomatized subcontinental lithospheric mantle. J. Earth Syst. Sci. 128 (8).
Schier, K., Bau, M., Münker, C., Beukes, N., Viehmann, S., 2018. Trace element and Nd isotope composition of shallow seawater prior to the Great Oxidation Event: Evidence from stromatolitic bioherms in the Paleoproterozoic Rooinekke and Nelani Formations, South Africa. Precambr. Res. 315, 92–102.
Shabani, M.B., Akagi, T., Masuda, A., 1992. Preconcentration of trace rare-earth elements in seawater by complexation with bis(2-ethylhexyl) hydrogen phosphate and 2-ethylhexyl dihydrogen phosphate adsorbed on a C18 cartridge and determination by inductively coupled plasma mass spectrometry. Anal Chem 64 (7), 737–743.
Shellnutt, J.G., Hari, K.R., Liao, A.-Y., Denyszyn, S.W., Vishwakarma, N., 2018. A 1.88 Ga giant radiating mafic dyke swarm across southern India and Western Australia. Precambr. Res. 308, 58–74.
Simonson, B.M., Goode, A.D.T., 1989. First discovery of ferruginous chert arenites in the early Precambrian Hamersley Group of Western Australia. Geology 17 (3), 269. https://doi.org/10.1130/0091-7613(1989)017<0269:FDOFCA>2.3.CO;2.
Tagliabue, A., Bopp, L., Dutay, J.-C., Bowie, A.R., Chever, F., Jean-Baptiste, P., Bucciarelli, E., Lannuzel, D., Remenyi, T., Sarthou, G., Aumont, O., Gehlen, M., Jeandel, C., 2010. Hydrothermal contribution to the oceanic dissolved iron inventory. Nat. Geosci. 3 (4), 252–256.

Taylor, S.R., McLennan, S.M., 1981. Chapter 21 The Rare Earth Element Evidence in Precambrian Sedimentary Rocks: Implications for Crustal Evolution. In: Kröner, A. (Ed.), Developments in Precambrian Geology. Elsevier, pp. 527–548.

Toth, J.R., 1980. Deposition of submarine crusts rich in manganese and iron. Geol. Soc. Am. Bull. 91 (1), 44. https://doi.org/10.1130/0016-7606(1980)91<44:DOSCRI>2.0.CO;2.

Trendall, A.F., 1972. Revolution in earth history. J. Geol. Soc. Aust. 19 (3), 287–311.

Trendall, A.F., Blockley, J.G., 1970. The iron formations of the Precambrian Hamersley Group western Australia with special reference to the associated crocidolite. Geological Survey Of Western Australia.

Veizer, J., Hoefs, J., Lowe, D.R., Thurston, P.C., 1989. Geochemistry of Precambrian carbonates: II. Archean greenstone belts and Archean sea-water. Geochim. Cosmochim. Acta 53 (4), 859–871.

Viehmann, S., Bau, M., Hoffmann, J.E., Münker, C., 2015. Geochemistry of the Krivoy Rog Banded Iron Formation, Ukraine, and the impact of peak episodes of increased global magmatic activity on the trace element composition of Precambrian seawater. Precambr. Res. 270, 165–180.

Walter, M.R., Goode, A.D.T., Hall, W.D.M., 1976. Microfossils from a newly discovered Precambrian stromatolitic iron formation in Western Australia. Nature 261 (5557), 221–223.

Wang, W., Bolhar, R., Zhou, M.-F., Zhao, X.-F., 2018. Enhanced terrestrial input into Paleoproterozoic to Mesoproterozoic carbonates in the southwestern South China Block during the fragmentation of the Columbia supercontinent. Precambr. Res. 313, 1–17.

Webb, G.E., Kamber, B.S., 2000. Rare earth elements in Holocene reefal microbialites: A new shallow seawater proxy. Geochim. Cosmochim. Acta 64 (9), 1557–1565.

Wilson, J.P., Fischer, W.W., Johnston, D.T., Knoll, A.H., Grotzinger, J.P., Walter, M.R., McNaughton, N.J., Simon, M., Abelson, J., Schrag, D.P., Summons, R., Allwood, A., Andres, M., Gammon, C., Garvin, J., Rashby, S., Schweizer, M., Watters, W.A., 2010. Geobiology of the late Paleoproterozoic Duck Creek Formation. Western Australia. Precambrian Research 179 (1-4), 135–149.

Zhang, Jing, Nozaki, Yoshiyuki, 1996. Rare earth elements and yttrium in seawater: ICP-MS determinations in the East Caroline, Coral Sea, and South Fiji basins of the western South Pacific Ocean. Geochim. Cosmochim. Acta 60, 4631–4644.

Zhu, X., Gao, Z., Wang, X., 2022. Shallow-water hydrothermal venting and the formation of Precambrian ironstones: Insights from the terminal-Paleoproterozoic Xuanlong ironstones in North China Craton. Precambrian Res 375, 106667. https://doi.org/10.1016/j.precamres.2022.106667.